Crack-free laser powder bed fusion by substrate design

Xufei Lu[a,*,†], Wenyou Zhang[b,*,†], Michele Chiumenti[a], Miguel Cervera[a], Bobby Gillham[b], Pengfei Yu[b], Shuo Yin[b], Xin Lin[c], Ramesh Padamati Babu[d], Rocco Lupoi[b,*]

[a] *International Centre for Numerical Methods in Engineering, Universidad Politécnica de Cataluña, Barcelona, Spain*

[b] *Trinity College Dublin (TCD), The University of Dublin, Department of Mechanical, Manufacturing & Biomedical Engineering, Parsons Building, Dublin, Ireland*

[c] *State Key Laboratory of Solidification Processing, Northwestern Polytechnical University, Xi'an, China*

[d] *Trinity College Dublin, The University of Dublin, School of Chemistry, CRANN, & AMBER, Dublin, Ireland*

Abstract: Additively manufactured components by laser powder bed fusion (LPBF) often suffer from stress-induced cracks (e.g. delamination), especially at the build-substrate interfaces where stiff mechanical constraints and large thermal gradients coexist. To reduce the probability of cracking, this work proposes an innovative strategy to optimize the geometry of the substrate by reducing its mechanical stiffness and, consequently, the stress accumulation during LPBF. To assess the feasibility of the strategy, a coupled thermo-mechanical finite element model, calibrated with the experimental evidence obtained from the LPBF metal deposition of a bridge-type structure, is used to predict the thermo-mechanical behavior of two T-shape AM parts built on (i) a typical solid substrate and (ii) a groove patterned substrate, respectively. The results show that several visible cracks appear at the interface between the build and the typical solid substrate due to stress concentration (up to 1600 MPa), while a crack-free component can be manufactured by adding grooves through the thickness of the substrate, without compromising the resulting microstructure and microhardness of the metallic materials with high crack sensitivity. The difference between the groove patterned substrate design with respect to the use of support structures used for printing cantilever structures is clarified to further justify the novelty of the proposed approach.

Key words: Laser powder bed fusion; Cracking; Structural optimization; Thermomechanical simulation.

* Corresponding author.

E-mail address: (X. Lu) xlu@cimne.upc.edu; (W. Zhang) zhangw7@tcd.ie; (R. Lupoi) lupoir@tcd.ie.

† These authors contributed equally to this work.

1 Introduction

Laser powder bed fusion (LPBF) additive manufacturing (AM) has been broadly utilized to fabricate complex and high-performance metallic components in different industrial sectors (e.g. aerospace or automotive) due to its intrinsic design and fabrication freedoms, if compared to traditional manufacturing technologies [1,2]. However, the metal deposition process in LPBF induces repeated heating and cooling cycles, and thus the material suffers from cyclic expansions and contractions. These deformations are usually restrained by a thick substrate in the practical AM processes and transform into large residual stresses in the manufactured part [3-5] and, cracking and delamination can occur eventually at some concentration points, contributing to the failure of the AM-build [6-8]. Thereby, this work aims at mitigating the residual stresses in LPBF and avoiding the occurrence of macro-cracking.

To better understand the thermo-mechanical behavior, a simple bar model shown in Fig. 1(a) is used to analyze the formation mechanisms of residual stresses in AM; the reader can refer to [9,10] for more details. Because of the heating and cooling cycles induced by the AM process, the AM-bar inevitably accumulates residual stresses and their magnitude is closely related to the peak temperature, T_{peak}, recorded at points a, c or e. T_Y denotes the yield temperature, which induces the yielding of the AM-bar during either heating or cooling process [10], and can be defined as:

$$T_Y = \left(\frac{A_{AM}}{A_{base}} + 1\right)\frac{\sigma_Y}{\alpha \cdot E} \tag{1}$$

where A_{AM} and A_{base} are the area of the central cross-section of the AM-bar and the Base-bar, respectively. E is the (temperature-dependent) Young's modulus, α is the (temperature-dependent) thermal expansion coefficient and σ_Y is the (temperature-dependent) yield stress. Hence, if $T_{peak} \leq T_Y$, no further residual stresses are formed; if $T_Y < T_{peak} \leq 2T_Y$, the magnitude of the residual stresses equals the absolute value of the segment $|od|$; if $2T_Y < T_{peak}$, the residual stresses reach the yield strength [9].

Normally, thick substrates (e.g. >10 mm) are employed in LPBF to minimize warpage of the fabricated components. However, a large stiffness prevents the thermal expansion of the cold substrate (i.e. compressive stresses are generated), as well as the contraction of the newly deposited layers (i.e. tensile stresses are generated) as shown in Fig. 1(b). Furthermore, as the molten pool solidifies, steep temperature gradients appear at the heat affected zone [11] and, consequently, large tensile stresses are rapidly developed, contributing to the solidification crack in the inter-dendritic region in some nickel-based and aluminum alloys [12-14]. Also, the longer the cooling process takes, the higher the residual tensile stresses are. This is particularly true in case of the LPBF process because the heating is very much localized close to the molten pool and the mechanical constraint induced by the (cold) substrate and the rest of the build (also cooled down during the recoating process) is higher compared to other AM technologies such as the directed energy deposition (DED) [15,16]. Thereby, macro cracks and delamination can easily be produced and particularly at the build-substrate interface (Fig. 1(b)).

To increase the cracking resistance in AM, most of the current strategies are focused on reducing the maximum thermal gradient (MTG), by optimizing scanning path [11], process parameters [16] and support structures [4], or by substrate preheating prior to the AM process [10]. However, their effect is limited because of the characteristic of LPBF: the applied high-energy beam heat source is directly responsible for the sharp MTG that appears [17-19]. A higher preheating temperature of the substrate favors a lower magnitude of residual stresses, but

it increases the oxygen content in the manufactured parts, and thus inferior mechanical properties are obtained [20]. Support structures are necessary when printing overhangs in LPBF, and some additional supports also are used in the non-cantilever building to facilitate substrate removal. However, this requires more raw material, increases both the manufacturing time and cost, and causes larger warpage or even cracks when using an inappropriate support design [21]. In addition, using these strategies in AM inevitably changes the thermal histories that the builds experience and affect their microstructural evolution and the resulting mechanical properties, narrowing the process window of metal AM and its industrial application [22,23].

From Eq. (1), it is clear that reducing the substrate area A_{base} can increase T_Y. Hence, reducing the mechanical constraining from the substrate can mitigate the formation of stress-induced cracking during AM processes. For the same reason, thinner substrates with a lower stiffness are beneficial with regard to reducing cracking, although causing larger part warpage.

In this work, a novel approach to optimize the stiffness of the conventional thick substrates is proposed. As shown in Fig. 1(c), by adding several grooves, the substrate is divided into different small regions while preserving the overall structural stiffness of the substrate. Therefore, the heat affected zone is allowed to expand during heating, avoiding that the thermal deformations transform into plastic strains; also, lower compressive stresses are generated thanks to the weak substrate constraint. Similarly, during the cooling period, an elastic recovery is favored, resulting in lower tensile stresses, and thus allowing for a crack-free AM fabrication.

This is the first time that a crack-free Ti-6Al-4V LPBF part is manufactured on a patterned substrate. Since the advantages of the proposed method follow from thermo-mechanics, it can be applied to the AM of different materials, especially those with high crack sensitivity, and more complex geometrical structures with stress-concentrating features.

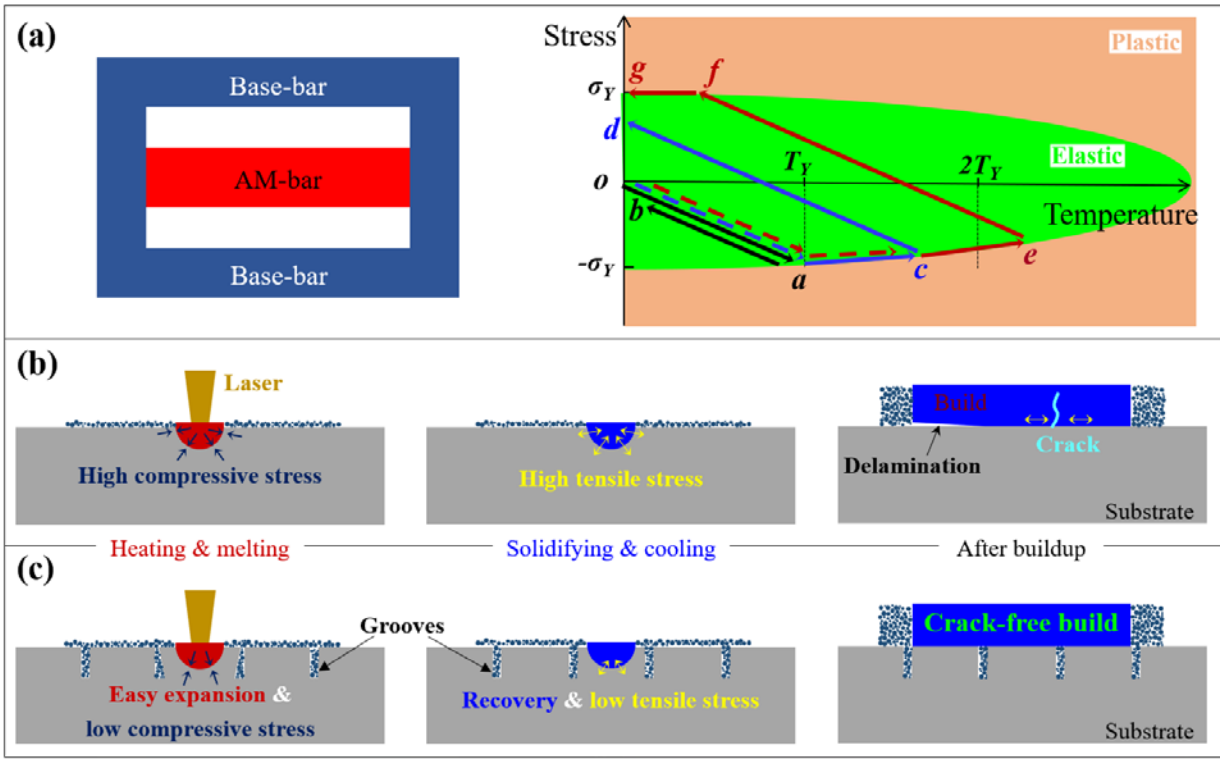

Fig. 1. (a) Three-bar model: the thermo-mechanical relationship of the AM-bar; (b) formation mechanism of residual stresses and cracks in AM; (c) crack prevention at the part-substrate interface by designing substrate structure.

2 Experimental conditions

Fig. 2 shows two Ti-6Al-4V T-shape parts with a nominal dimension of 40×24×10 mm^3 printed by a Realizer SLM50 LPBF system in the AMBER AR-Lab in TCD. This AM machine is equipped with a CW fibre laser with a wavelength of 1064 nm. The Ti-6Al-4V ELI powder (grade 23) with particle size ranges from 15 to 45 µm is used for LPBF manufacturing; its chemical composition is shown in Table 1. For comparison purpose, two annealed cylindrical Ti-6Al-4V substrates with a size of Ø70×10 mm^3 are used. The first one is kept in its original format while the second one is characterized by several grooves (Fig. 2). Before printing, the 5 mm deep and 0.25 mm wide grooves on the substrate are cut by a wire electric discharge machining (Excetez V440G EDM). The AM builds are carried out under an argon atmosphere with a gas flow speed of 65 L/min and the oxygen level is always kept below 0.24%. An alternating scanning path is used as shown by the red lines in Fig. 2(b). Typically, the longitudinal stresses along the scanning path are mainly responsible for the residual stresses; thus, to reduce the risk of cracking, the grooves are cut following a pattern perpendicular to the printing path. Before depositing the first layer in LPBF, the grooves are filled with loose powder by the recoater to facilitate the powder spreading process of the subsequent layers (see Fig. 1(c)).

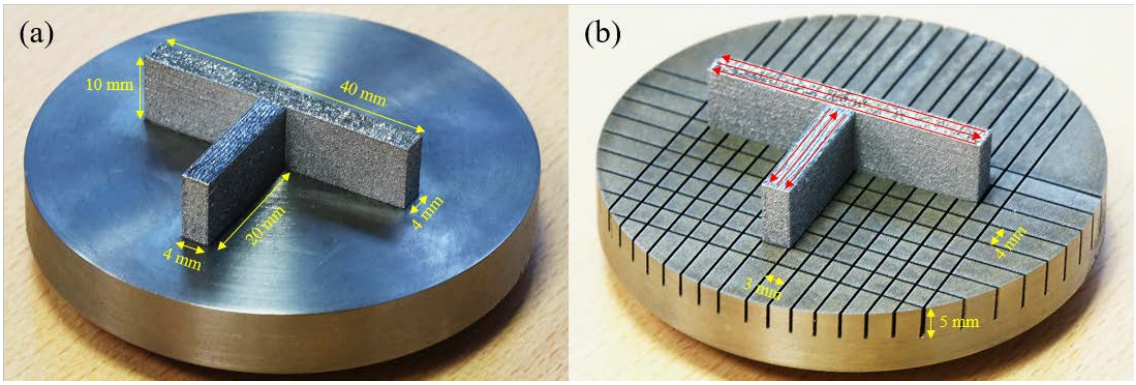

Fig. 2. Two T-shape components fabricated on (a) the typical (no grooves) and (b) the patterned (with grooves) substrates.

Table 1. Composition analysis of Ti-6Al-4V powder used for printing (wt%) [20].

N	C	H	Fe	O	Al	V	Ti
0.02	0.01	0.003	0.17	0.08	6.4	3.9	Bal.

In addition, a Ti-6Al-4V bridge geometry is fabricated by a KUL-SLM powder bed machine equipped by a Yb:YAG laser with a wavelength of 1085 nm, as shown in Fig. 3. Like with the T-shapes, several longitudinal (along X-direction) scan vectors with a length of 20 mm were used to build the bridge without support. The details of the fabrication of this bridge structure are given in [24].

The process parameters used for fabricating the two LPBF parts are listed in Table 2.

After the LPBF process was completed, the bridge is cut from the substrate to measure the curling angle θ due to stress relaxation (see Fig. 3) and this angle is used to validate the numerical model; the T-shape samples are cut by EDM to analyze the crack formation and the microstructure distribution. Vickers microhardness of the T-shape deposits is measured using a Mitutoyo MVK-H1 hardness testing machine. In each sample, 10 points are considered to get an average value. Both an optical microscope and a scanning electron microscopy are employed to analyse the Ti-6Al-4V microstructure of all the T-shape samples.

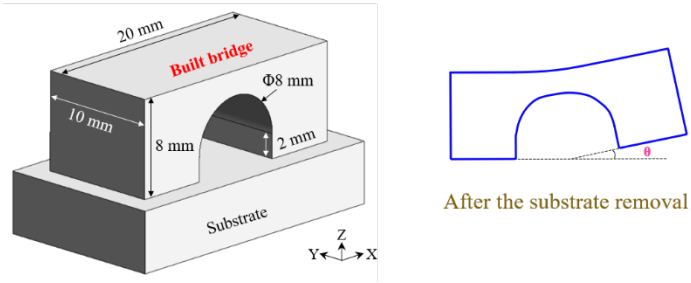

Fig. 3. The size of the bridge structure and the scheme of its bending warpage after the substrate removal, adapted from [24].

Table 2. LPBF processing parameters for printing the T-shape and bridge parts.

	Laser power (W)	Scan speed (mm/s)	Hatch spacing (μm)	Layer thickness (μm)	Laser spot diameter (μm)
T-shape	90	500	80	25	170
Bridge [24]	42	225	74	30	80

3 Computational simulation

In this work, an in-house 3D thermo-mechanical finite element (FE) software, *COMET*, is employed to perform the LPBF modelling [25]. The sequentially coupled thermo-mechanical modelling, where the temperature field is independent of the stress field, is performed as follows: (i) for each time-step, the transient thermal analysis is conducted first; (ii) then the mechanical analysis is solved by importing the calculated temperature field. Details of this thermo-mechanical coupled software and framework for AM can be found in the authors' previous publications, validated by a number of in-situ thermo-mechanical experimental measurements [18,26,27].

3.1 Thermal analysis for AM

In the sequentially coupled thermo-mechanical modelling, the heat transfer process is independent of the mechanical behavior of material and the governing equation for the transient thermal analysis can be expressed as:

$$\dot{H} = -\nabla \cdot \mathbf{q} + \dot{Q} \tag{2}$$

where $\dot{H}$ for enthalpy rate, $\mathbf{q}$ for heat flux, $\dot{Q}$ for heat source (per unit of volume), which can be calculated by the total laser input $\dot{P}$, the laser absorption efficiency η_p, and the volume of the molten pool $V_{pool}^{\Delta t}$:

$$\dot{Q} = \frac{\eta_p \dot{P}}{V_{pool}^{\Delta t}} \tag{3}$$

The thermal transfer mechanisms that are considered in the thermal analysis include: heat conduction to the substrate and previously deposited material, conduction to the surrounding powder, convection, and radiation from the top surface to the environment before the next layer is added. The heat flux $\mathbf{q}$ due to heat conduction is formulated via Fourier's law:

$$\mathbf{q} = -k\nabla T \tag{4}$$

where k and ∇T are the (temperature-dependent) thermal conductivity and the thermal gradient, respectively.

The heat dissipation due to convection from the top surface of the build to the surrounding environment is defined by Newton's law:

$$q_{conv} = h_{conv}(T - T_{room}) \tag{5}$$

where h_{conv} is the convective Heat Transfer Coefficient (HTC), T is the surface temperature of the workpiece and T_{room} is the room temperature.

The heat loss caused by the radiation q_{rad} is computed by Stefan-Boltzmann's law:

$$q_{rad} = \varepsilon_{rad}\sigma_{rad}(T^4 - T_{room}^4) \tag{6}$$

where ε_{rad} and σ_{rad} are the surface emissivity and the Stefan-Boltzmann constant, respectively.

3.2 Mechanical analysis

The stress analysis is performed after the thermal analysis, which is implemented by computationally solving the balance of momentum and the continuity equations:

$$\nabla \cdot \mathbf{s} + \nabla p + \mathbf{b} = 0 \tag{7}$$

$$(\nabla \cdot \mathbf{u} - e^T) - \frac{p}{K(T)} = 0 \tag{8}$$

where $\mathbf{b}$ is the body force (per unit of volume), $K(T)$ is the (temperature-dependent) bulk modulus, and the Cauchy stress tensor $\boldsymbol{\sigma}$ can be split into its spherical (pressure) p and deviatoric $\mathbf{s}$ parts:

$$\boldsymbol{\sigma} = p\boldsymbol{I} + \mathbf{s}(\mathbf{u}) \tag{9}$$

The thermal deformation e^T is determined by:

$$e^T(T, f_S) = e^{cool}(T) + e^{pc}(f_S) \tag{10}$$

where $e^{cool}(T)$ and $e^{pc}(f_S)$ are the thermal expansion and thermal shrinkage in the liquid-to-solid phase transformation, as a function of the initial temperature T_0 and the solid fraction f_S, and can be expressed as:

$$e^{cool}(T) = \alpha(T)(T - T_0) \tag{11}$$

$$e^{pc}(f_S) = \beta f_S \tag{12}$$

where α and β are the (temperature-dependent) thermal expansion and the shrinkage coefficients, respectively.

The mechanical equations in Eqs. (7) and (8) are determined by both the displacement $\mathbf{u}$ and the pressure field p, and they are suitable for both compressible and the fully incompressible (isochoric) material behavior.

With the repeated heating-cooling cycles in LPBF, the temperature of material fluctuates up and down between room temperature T_{room} and temperatures above the melting point (T_{melt}). Thus, the materials must be featured in its solid, mushy and liquid phases. A *J2*-thermo-elasto-visco-plastic model is adopted in the solid phase, from T_{room} to the annealing temperature T_{anneal}. All the material properties are assumed as temperature-dependent. The von-Mises yield-surface can be formulated as:

$$\Phi(\mathbf{s}, q_h, T) = \|\mathbf{s}\| - \sqrt{\frac{2}{3}}\left[\sigma_y(T) - q_h\right] \tag{13}$$

where σ_y is the temperature-dependent yield stress that is accounted for the thermal softening and q_h is the stress-like variable controlling the isotropic strain-hardening, which can be defined as:

$$q_h(\xi, T) = -\left[\sigma_\infty(T) - \sigma_y(T)\right]\left[1 - e^{-\delta(T)\xi}\right] - h(T)\xi \tag{14}$$

where ξ and σ_∞ are the isotropic strain-hardening variable and the temperature-dependent saturation flow stress, respectively, while δ and h are the temperature-dependent parameters to model the exponential and linear hardening laws, respectively.

The deviatoric counterpart of Cauchy's stress tensor $\mathbf{s}$ can be expressed as follows:

$$\mathbf{s} = 2G(\mathbf{e} - \mathbf{e}^{vp}) \tag{15}$$

where G is the (temperature-dependent) shear modulus, $\mathbf{e}$ is the total (deviatoric) strain, which is obtained from the total strain tensor $\boldsymbol{\varepsilon}(\mathbf{u}) = \nabla^{sym}(\mathbf{u})$, and $\mathbf{e}^{vp}$ is the visco-plastic strain. The evolution laws of both the visco-plastic

strain tensor and the isotropic strain-hardening variable are obtained from the principle of maximum plastic dissipation:

$$\dot{\mathbf{e}}^{vp} = \dot{\gamma}^{vp} \frac{\partial \Phi(\mathbf{s}, q_h)}{\partial \mathbf{s}} = \dot{\gamma}^{vp} \frac{\mathbf{s}}{\|\mathbf{s}\|} = \dot{\gamma}^{vp} \mathbf{n} \tag{16}$$

$$\dot{\xi} = \dot{\gamma}^{vp} \frac{\partial \Phi(\mathbf{s}, q_h)}{\partial q_h} = \sqrt{\frac{2}{3}} \dot{\gamma}^{vp} \tag{17}$$

where **n** stands for the normal to the yield surface, and $\dot{\gamma}^{vp}$ is the visco-plastic multiplier and can be expressed as:

$$\dot{\gamma}^{vp} = \langle \frac{\Phi(\mathbf{s}, q_h)}{\eta} \rangle^{\frac{1}{m}} \tag{18}$$

where $\langle \cdot \rangle$ are the Macaulay brackets, and m and η are the temperature-dependent rate sensitivity and plastic viscosity, respectively.

Note that when the temperature of material gets close to T_{anneal} the yield limit σ_y tends to be 0. Thereby, the deviatoric Cauchy stress reduces to:

$$\mathbf{s} = \eta (\dot{\gamma}^{vp})^m \mathbf{n} = \eta_{eff} \dot{\mathbf{e}}^{vp} \tag{19}$$

where $\eta_{eff} = \eta (\dot{\gamma}^{vp})^{m-1}$ is the effective viscosity. Thus, the material is featured by a purely viscous law when the temperature is higher than T_{anneal} [28]. A non-Newtonian behavior with $m > 1$ is adopted for the mushy phase (from T_{anneal} to T_{melt}), while a Newtonian law, $m = 1$, is featured for the liquid phase (for $T > T_{melt}$).

3.3. Computational modelling of LPBF

To simulate the LPBF process, a time discretization framework is needed. The time-marching scheme is characterized by a time step, $\Delta t = t^{n+1} - t^n$. Thereby, the molten pool is allowed to move in a step-by-step manner based on the pre-defined scan path from the location at time t^n to that at time t^{n+1}. During this time interval, the heat is input into the elements that belong to the molten-pool volume and then the scanned powder conforms as the AM deposit.

Thereby, the software parses the same input file (Common Layer Interface format) following the actual building sequence as adopted to inform the physical LPBF system. The *birth-death-element* technique is utilized to gradually activate the elements corresponding to each newly deposited layer. Therefore, the numerical strategy for the LPBF process requires an ad-hoc procedure to categorize the elements into: *active*, *inactive*, and *activated* elements. At each time step, an octree-based searching algorithm is employed to search the elements belonging to the molten pool (*active*) and to the new deposit (*activated*). The current computational domain consists of both *active* and *activated* elements, while the *inactive* elements are neither assembled nor computed into the global matrix of the analysis [25]. For the convenience of computational modelling, the powder bed surrounding the build is excluded in the computational domain while its effect is considered using an equivalent boundary condition: the HTC by conduction between the powder bed and the AM-build is set to 5 W/(m^2·ºC) [29].

Fig. 4 shows different 3D structures of LPBF components and the corresponding meshes generated by the pre-post-processor *GiD* [30]. Fig. 4(a) depicts the bridge structure used to validate the FE thermo-mechanical model. Fig. 4(b-d) show the solid T-shape structure built on the typical and patterned substrates and the additional supports, respectively, in order to distinguish their effect on the mechanical response of AM-parts. Figs. 4(e) and (f) display the same cantilever T-shape structures with supports, manufactured on the patterned and typical substrates,

respectively, to demonstrate the effectiveness of substrate design. Table 3 lists the dimensions of all the LPBF-components presented in Fig. 4 and the corresponding numbers of hexahedral elements and nodes. To reduce the computational cost while preserving high accuracy, ten physical layers are lumped into a computational one [31,32], so the mesh sizes are set as 0.33×0.33×0.3 mm^3 for the bridge structure and 0.5×0.5×0.25 mm^3 for the T-shape parts. A coarser mesh is adopted for the substrate based on a previous mesh convergence study [29].

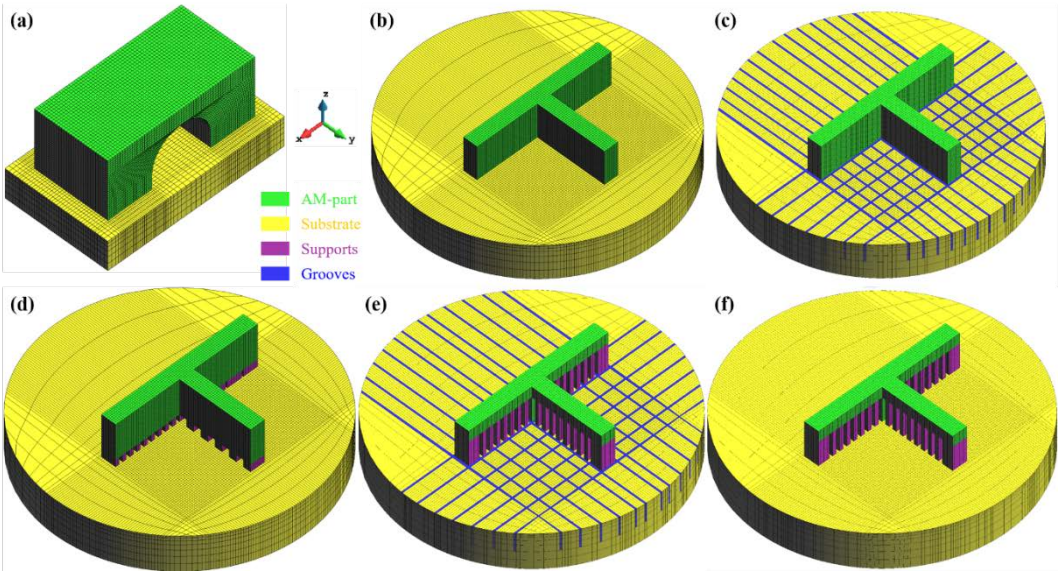

Fig. 4. FE models: (a) the bridge part; the T-shape parts built on the (b) typical and (c) patterned substrates and (d) on the additional supports with a height of 2 mm and three different thicknesses of 1, 2 and 4 mm; (e) the T-shape cantilever part with 7 mm high supports manufactured on the patterned substrate; (f) the T-shape cantilever part with 7 mm high supports manufactured on the typical substrate. (The grooves in the patterned substrate are filled by loose powder in LPBF).

Table 3. Part sizes and the numbers of FE elements and nodes.

	Size of LPBF-parts (mm^3)	Number of elements	Number of nodes
Bridge part	20×10×8	69,240	76,902
T-shape on typical substrate	40×22×10	78,328	90,432
T-shape on patterned substrate	40×22×10	78,328	90,432
T-shape on additional supports	40×22×10 + 40×22×2 (supports)	83,320	97,632
T-shape cantilever on patterned substrate	40×22×10 (support height: 7)	67,128	84,438
T-shape cantilever on typical substrate	40×22×10 (support height: 7)	67,128	67,128

3.4 Material properties and boundary conditions

Table 4 lists the (temperature-dependent) thermodynamic properties of Ti-6Al-4V used for both the AM-build and the substrate in the computational modelling [5]. A higher heat conductivity is defined when $T > T_{melt}$ to consider the effect of the convective flow inside the molten pool [16]. In the case of the patterned substrate, the thermal and mechanical properties of materials for the groove elements (filled by loose powder) are assumed as 5% and 0.01% of the solids, respectively.

To simulate the LPBF process, the heat dissipation through convection and radiation is considered for all the free surfaces of the LPBF-parts, being the corresponding HTCs set to 12.7 W/(m^2·ºC) and 0.35, respectively [33]. The laser efficiency is set as 0.4 [33] and the room temperature is fixed at 27ºC in all simulations.

The mechanical boundary conditions in simulation follows the actual LPBF experimental setups: the whole bottom surface of the substrate used to fabricate the bridge structure is clamped, while a small circular area (Ø10 mm) in the central region of the lower surface of the substrate is fixed for the T-shape samples.

Table 4. Thermodynamic properties of Ti-6Al-4V [5].

Temperature (ºC)	Thermal conductivity (W/(m·°C))	Density (kg/m^3)	Heat capacity (J/(kg·°C))	Poisson's ratio	Elastic limit (MPa)	Thermal expansion coefficient (μm/(m·°C))	Young's modulus (GPa)
20	7	4420	546	0.345	850	8.78	110
205	8.75	4395	584	0.35	630	10	100
500	12.6	4350	651	0.37	470	11.2	76
995	22.7	4282	753	0.43	13	12.3	15
1100	19.3	4267	641	0.43	5	12.4	5
1200	21	4252	660	0.43	1	12.42	4
1600	25.8	4198	732	0.43	0.5	12.5	1
1650	83.5	3886	831	0.43	0.1	12.5	0.1
2000	83.5	3818	831	0.43	0.01	12.5	0.01

4 Results and discussion

4.1 FE model validation

The thermo-mechanical model used for the AM analysis has been validated in previous works to optimize both process parameters and material properties, but for different geometries and parameters [18,26]. For ensuring the simulation accuracy in this study, the model is further calibrated by comparing the experimental measurements reported in [24]. Fig. 5(a) shows the predicted curling angle of 2.76º, by plotting the Z coordinates of nodes on the central line of the bottom surface of the bridge structure. The calculated angle agrees remarkably well with the experimental evidence (about 2.8º) [24], within less than 2% difference.

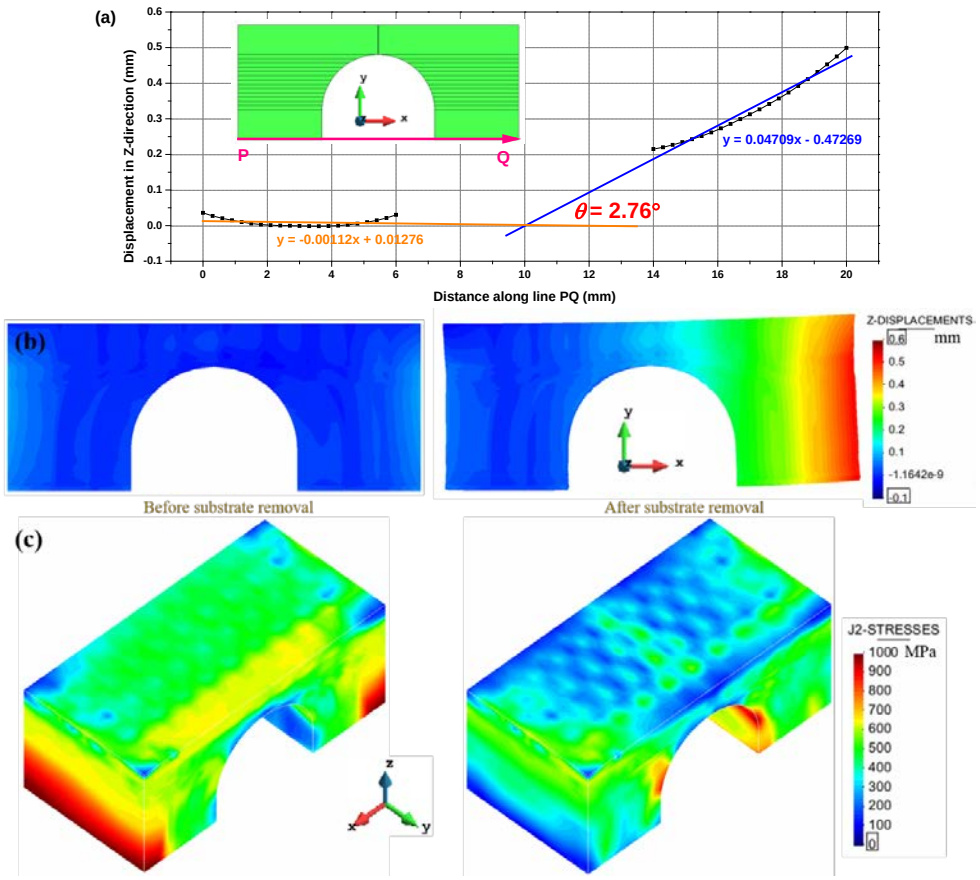

Fig. 5. (a) The calculated curling angle α of the bridge structure after the substrate removal; (b) the vertical displacement profile and (c) the residual Von Mises fields before and after the substrate removal.

Fig. 5(b) and (c) present the profiles of the vertical displacement and the residual Von Mises stresses before and after the substrate removal, respectively. Observe that before cutting the substrate, the part distortion is quite small (less than 0.1 mm) while the residual stresses are high (up to 1000 MPa) at the basement of the bridge deposit. Once the substrate is removed, the residual stresses are dramatically released by the development of plastic deformation, up to 0.53 mm at the end of the bridge. Similar results have been previously reported in [32,34-36].

4.2 Effect of substrate stiffness on cracking

By cutting both the part and the substrate through a plane perpendicular to their interface, it is more visible to check if any cracks occur after the cooling for the two base-plate geometries (i.e. with and without grooves). The corresponding cross-sections are shown in Fig. 6. Note that in the typical substrate (without grooves) visible cracks (delamination) with a length of more than 2 mm appear at the basement of the T-shape part (positions Ⅰ and Ⅱ), as shown in Fig. 6(a). Also, a small crack is developed at the end of the short-wall (position Ⅲ). However, it can be seen from Fig. 6(b) that no cracks are found when the groove pattern is included in the substrate. Moreover, a good metallurgical quality is preserved in both configurations.

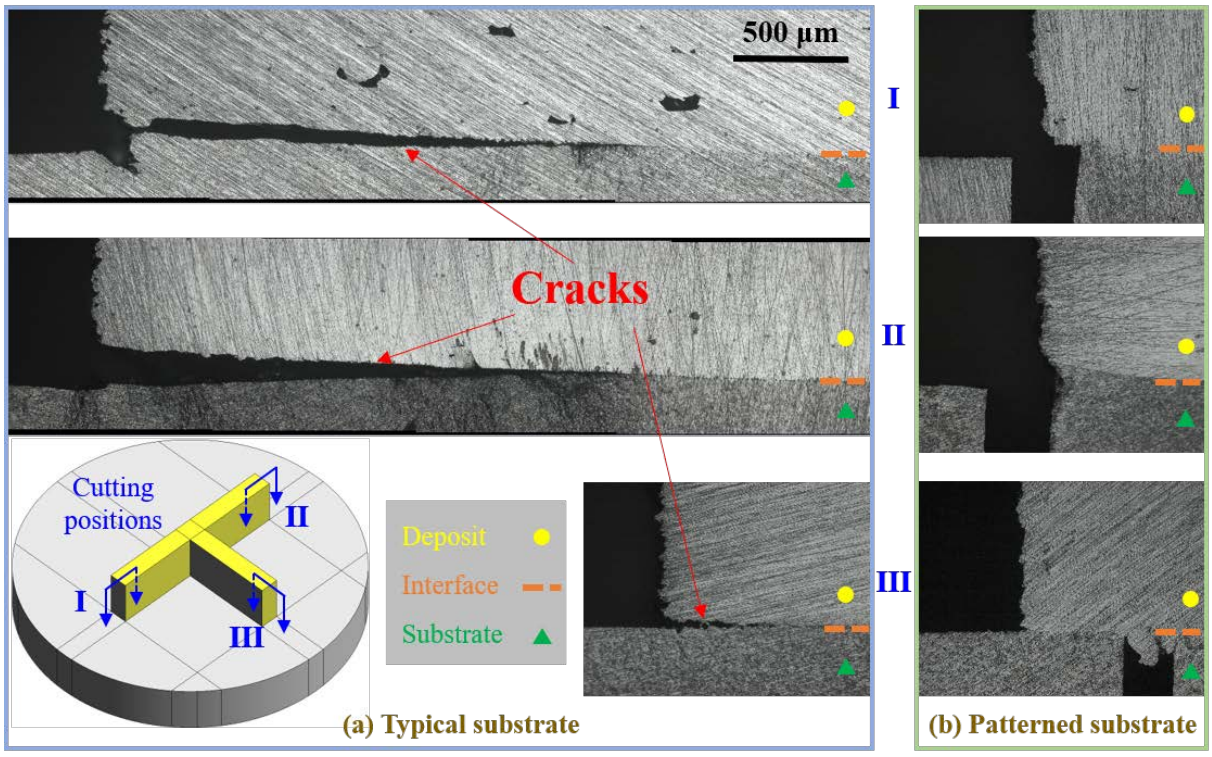

Fig. 6. T-shape components manufactured on two different substrates: cross-sections perpendicular to the build-substrate interface.

Fig. 7 shows the stress distributions in three orthogonal directions at the part-substrate interfaces. It is interesting to observe that by increasing the number of the deposited layers, the tensile stresses in the longitudinal (σ_{xx} in Fig. 7(a)), transversal (σ_{yy} in Fig. 7(c)) and vertical (σ_{zz} in Fig. 7(e)) directions initially rise up during the deposition of the first 20 layers and then tend to stabilize. Undoubtedly, such high tensile stresses (up to 1600 MPa) contribute to the crack initiation and propagation at the basement of the T-shape part (Fig. 6(a)). However, this is not the case for the groove-patterned substrate because the stress concentration at both extremes of the part is avoided by reducing the local stiffness of the thick substrate (see Fig. 7(b) and 7(d)). Fig. 8 shows the evolution of

the Von Mises stress field for both cases. Obviously, the proposed substrate design is able to drastically reduce (approximately 50%) the residual stresses (particularly in the bottom region), eliminating the cracking risk during LPBF. The predicted stress concentrations at the basement of the T-shape builds are similar with the experimentally measured results of the Ti-6Al-4V LPBF-parts in previous reports [37,38].

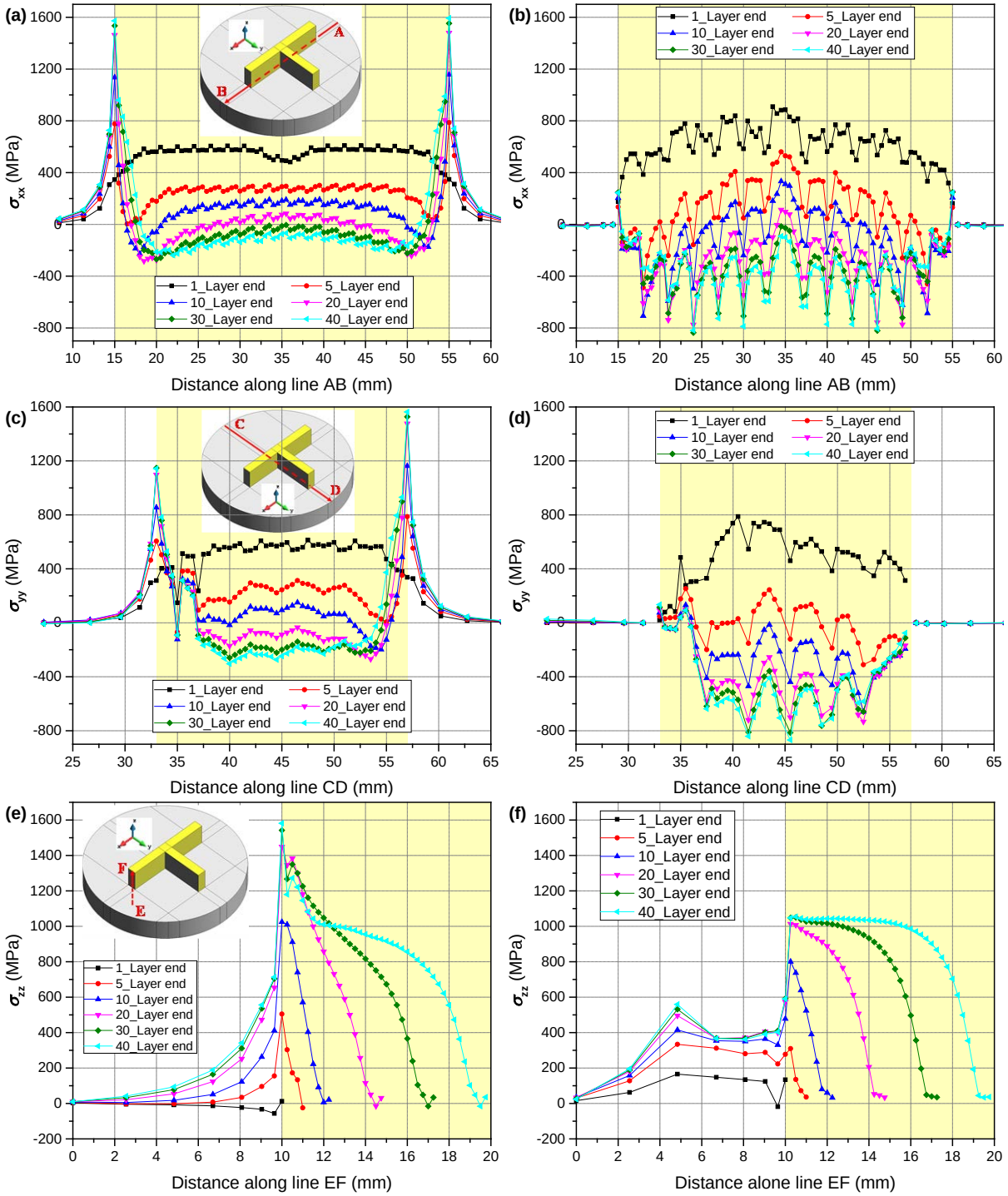

Fig. 7. Evolution of the predicted stresses of the T-shape parts in three orthogonal directions: (a,c,e) typical substrate; (b,d,f) patterned substrate.

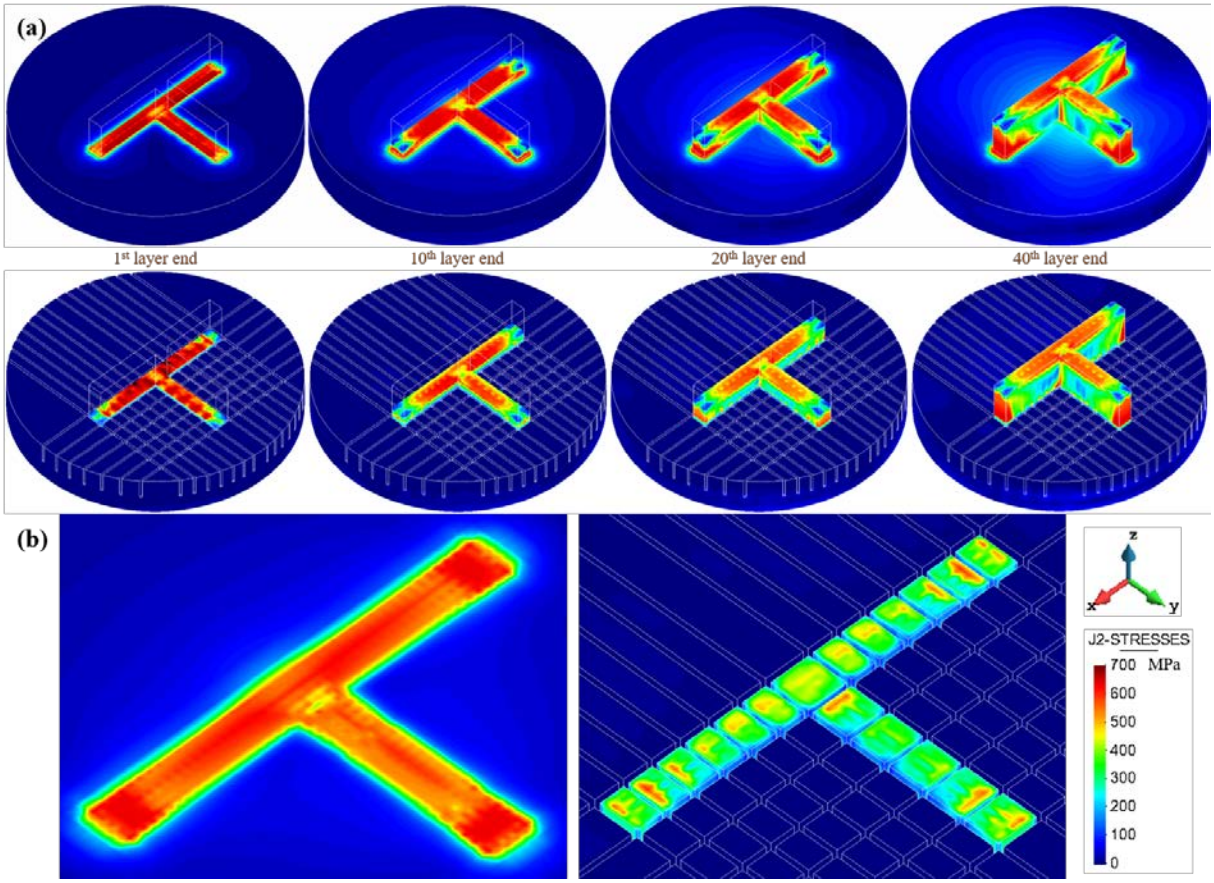

Fig. 8. (a) Evolution of the simulated Von Mises stress field of the T-shape parts fabricated on two different substrates; (b) enlarged part-substrate interface after the deposition of the 10th layer.

4.3 Comparison between substrate design and support assistance

To further clarify the novelty of substrate design and to distinguish it from the support assistance normally used in printing cantilever geometries in LPBF [21,39,40], a comprehensive comparison between them is performed in this section based on the mechanical analysis of two solid T-shape structures: without (Fig. 4(b)) and with (Fig. 4(d)) additional supports.

The same T-shape structure without cantilever presented in Section 4.2 is virtually fabricated on the additional supports to check if stress reduction and crack prevention can be achieved by applying sacrificial support structures. Figs. 9 and 10 show the stress evolution in three orthogonal directions and the development of the Von Mises stress field of the T-shaped part with supports, respectively. Note that after the support structure is printed and before printing the T-shape build, the thermal stresses have accumulated at the basement of the supports, especially for the thicker supports (up to 1100 MPa in Fig. 9(a)). This is not the case for the substrate design in which the substrate is stress-free before LPBF (Fig. 2(b)). Furthermore, once new layers are stacked on the supports to form the T-shape build, the stress distributions pronouncedly change. Stress concentrations appear at the bottom ends of the supports and the build, and their magnitude is up to 1500 MPa (Fig. 9), easily triggering cracks at these corners, similarly to the case of the typical substrate (Figs. 6 and 7). Comparison of the T-shape parts printed on the typical substrate without (Fig. 7) and with (Fig. 9) additional supports shows that the support structure has an insignificant effect on mitigating residual stresses. In detail, the maximum residual stress in the case with support (1500 MPa) is only 6.25% less than that without support (1600 MPa). Additionally, the residual stress

accumulations at the built basement are hardly controlled by changing the thickness of the support legs (Fig. 10). Thereby, using additional supports to lower the crack risk is not effective and they increase both manufacturing time and cost.

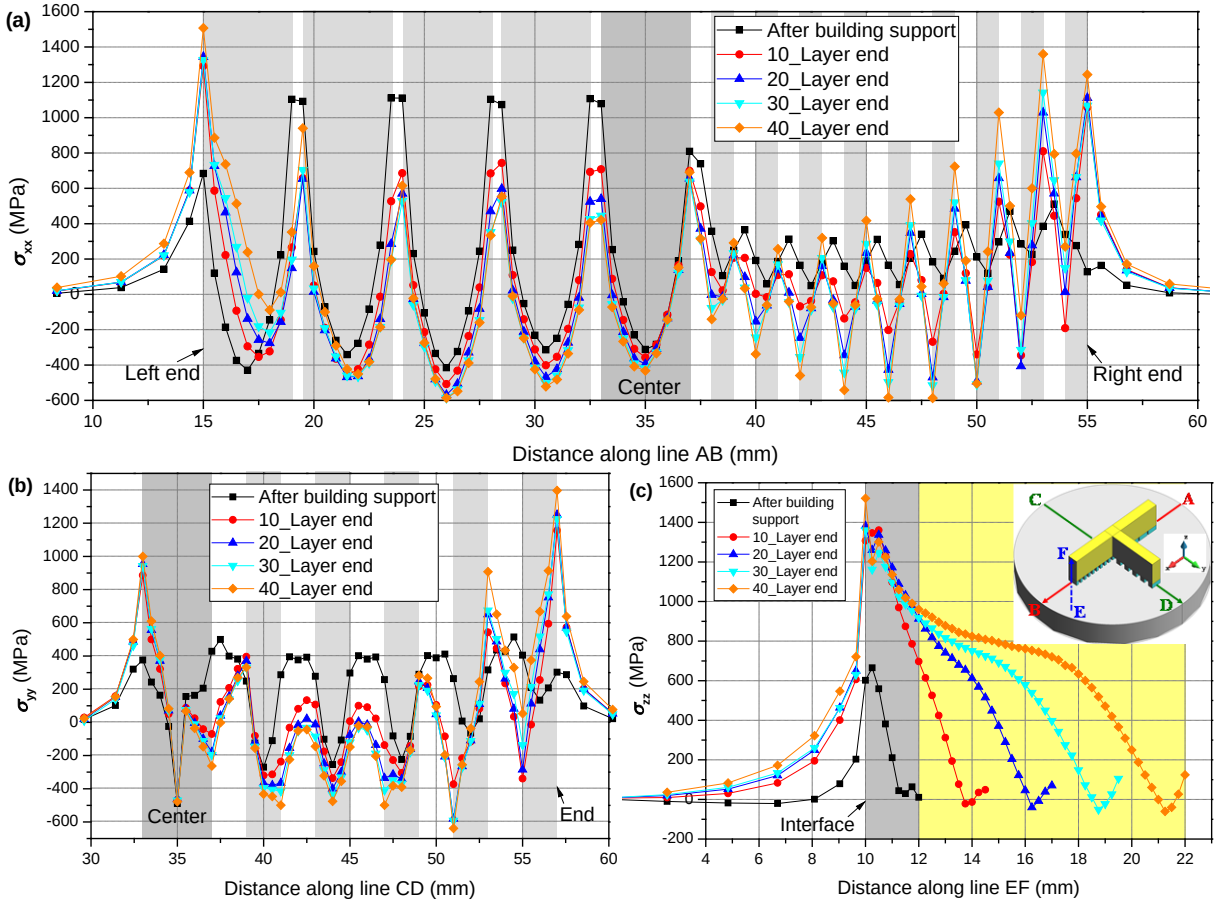

Fig. 9. Evolution of the predicted stresses of the T-shape part fabricated on the additional supports: (a) σ_{xx} along the line AB; (b) σ_{yy} along the line CD; (c) σ_{zz} along the line EF.

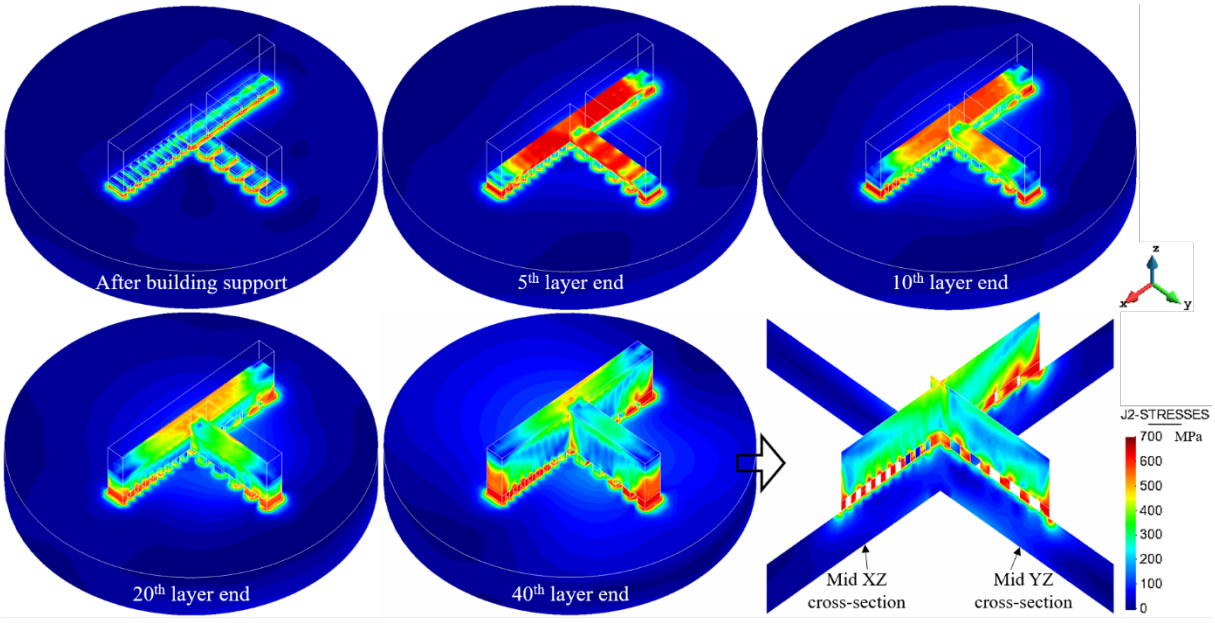

Fig. 10. Evolution of the predicted Von Mises stress contours of the T-shape part fabricated on the additional supports.

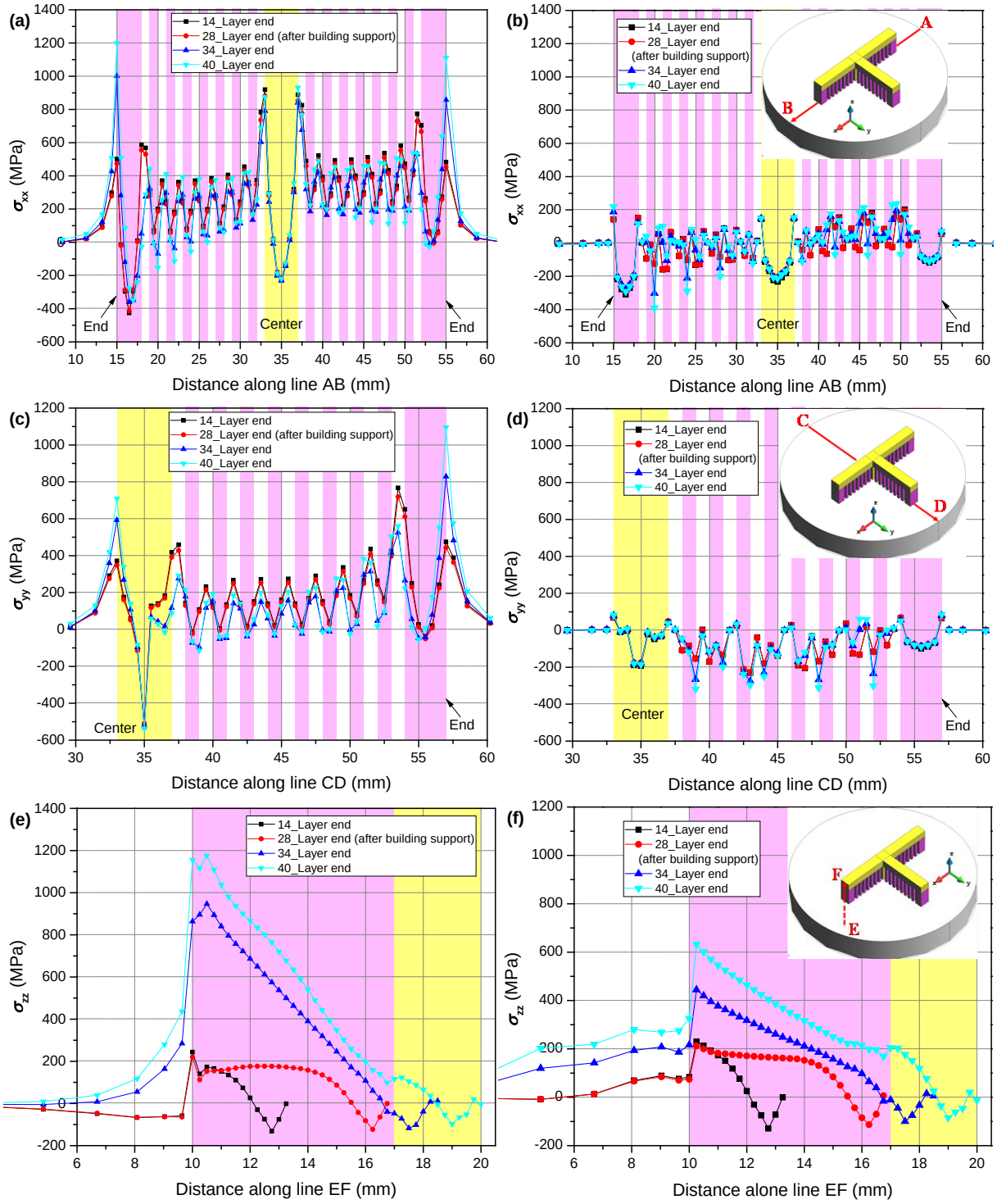

Fig. 11. Comparison of the predicted stress evolution of the T-shape cantilever structure deposited on the (a, c, e) typical and (b, d, f) patterned substrates: (a) and (b) σ_{xx} along the line AB; (c) and (d) σ_{yy} along the line CD; (e) and (f) σ_{zz} along the line EF.

4.4 Effect of substrate design on printing cantilever structures

In this section, a new geometry, a central short pillar with three cantilevers, is additively manufactured with the assistance of the necessary supports. Here, the mechanical behavior of two T-shape cantilever parts deposited on the patterned (Fig. 4(e)) and typical (Fig. 4(f)) substrates, respectively, is compared, as shown in Figs. 11 and 12. In this case, it is still possible to apply the substrate design strategy to avoid the stress-induced cracks in LPBF.

Observe that the typical substrate yields high stress concentrations at the bottom ends of the built part. Nevertheless, the stress level is much lower for the patterned substrate. Also, the substrate design strategy provides more design freedom and support optimization in LPBF of cantilever structures.

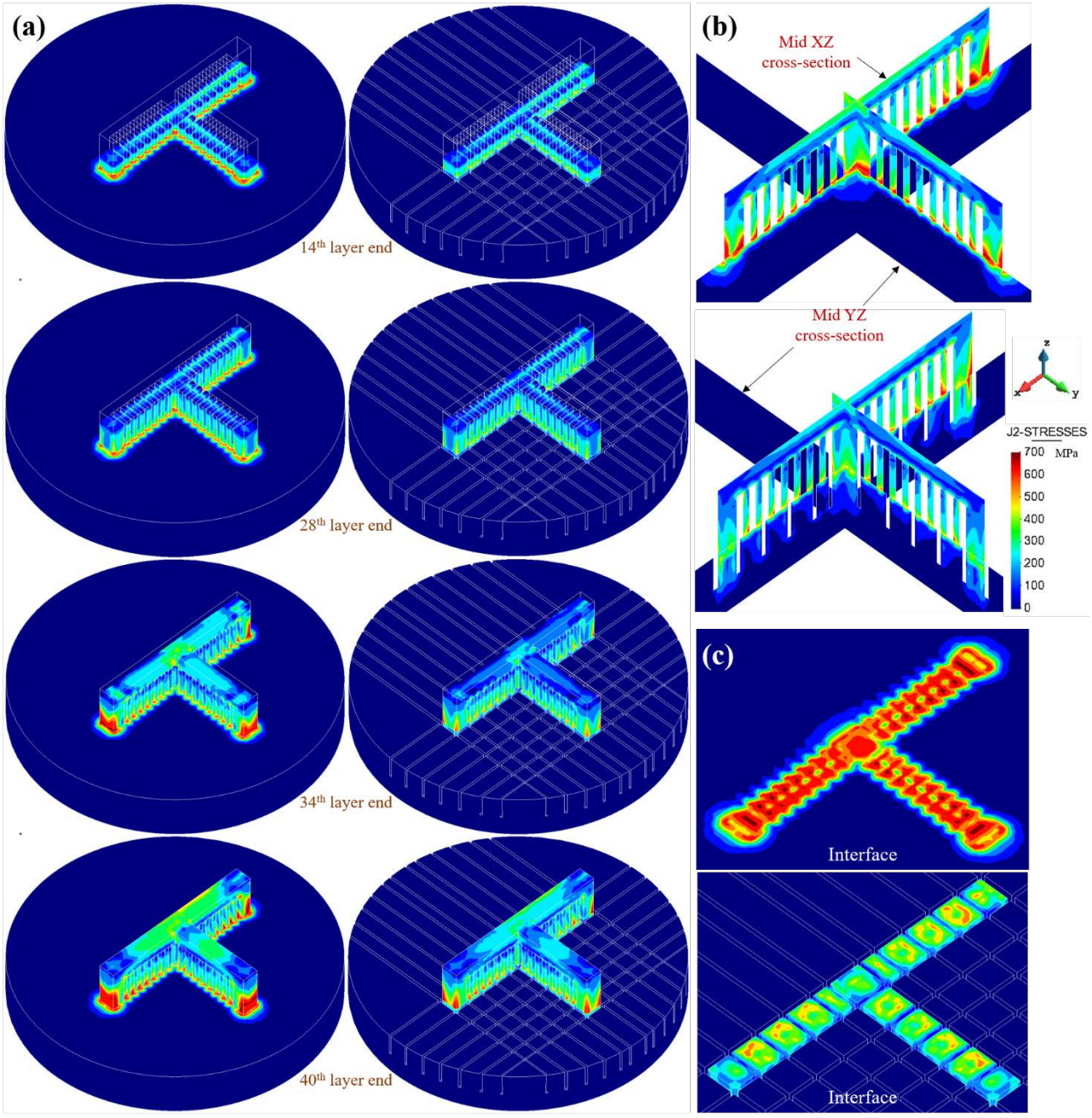

Fig. 12. (a) Comparison of the Von Mises stress evolution of the T-shape cantilever structure deposited on the typical and patterned supports; (b) Residual stresses at the mid XZ and YZ cross-sections; (c) Residual stresses at the build-substrate interface.

It should be mentioned that in this work the selected substrate ($\Phi 70 \times 10$ mm^3) is small and presents a reduced clamping condition. Thus, it is characterized by a small stiffness if compared to other industrial solutions. Moreover, the Ti-6Al-4V alloy used has a lower crack sensitivity than some other aluminum or Inconel super-alloys [41-43]. Thus, the proposed solution can be even more attractive in those AM configurations, offering a proven mitigation of residual stresses and a visible reduction of the cracking risk in metal AM processing.

4.5 Effect of substrate design on microstructure and microhardness

In this section, the microstructures and micro-hardness are analyzed to check against the possible drawbacks of adopting the proposed groove pattern in LPBF processes. Figs. 13 and 14 compare the temperature histories and the corresponding microstructures and microhardness at the center and different building heights of the short-wall of the T-shape components fabricated with the two substrates, respectively. Note that both substrates produce similar microstructures and resulting microhardness because the two AM components experience very close temperature histories at these positions (see Fig. 13). This can be foreseen based on the following facts. The metallurgical evolution of Ti-6Al-4V strongly depends on the thermal histories in the high-temperature stage (e.g. >600ºC) rather than on the low-temperature stage [44]. On the one hand, the molten-pool shape, its temperature distribution and its rapid solidification during cooling are almost the same for the typical and patterned substrates due to the same process parameters used and, thus, the initially solidified microstructures are quite similar. On the other hand, unlike DED, the LPBF process without substrate preheating is characterized by a weak thermal accumulation and the Ti-6Al-4V microstructures do not change under such lower-temperature intrinsic heat treatment (see Fig. 13). Furthermore, the microhardness results as a function of microstructure [45] are similar for both cases.

Adding grooves in the substrate is purely a modification of the mechanical constraining and its influence on the heat dissipation and the temperature distribution in the build is very weak.

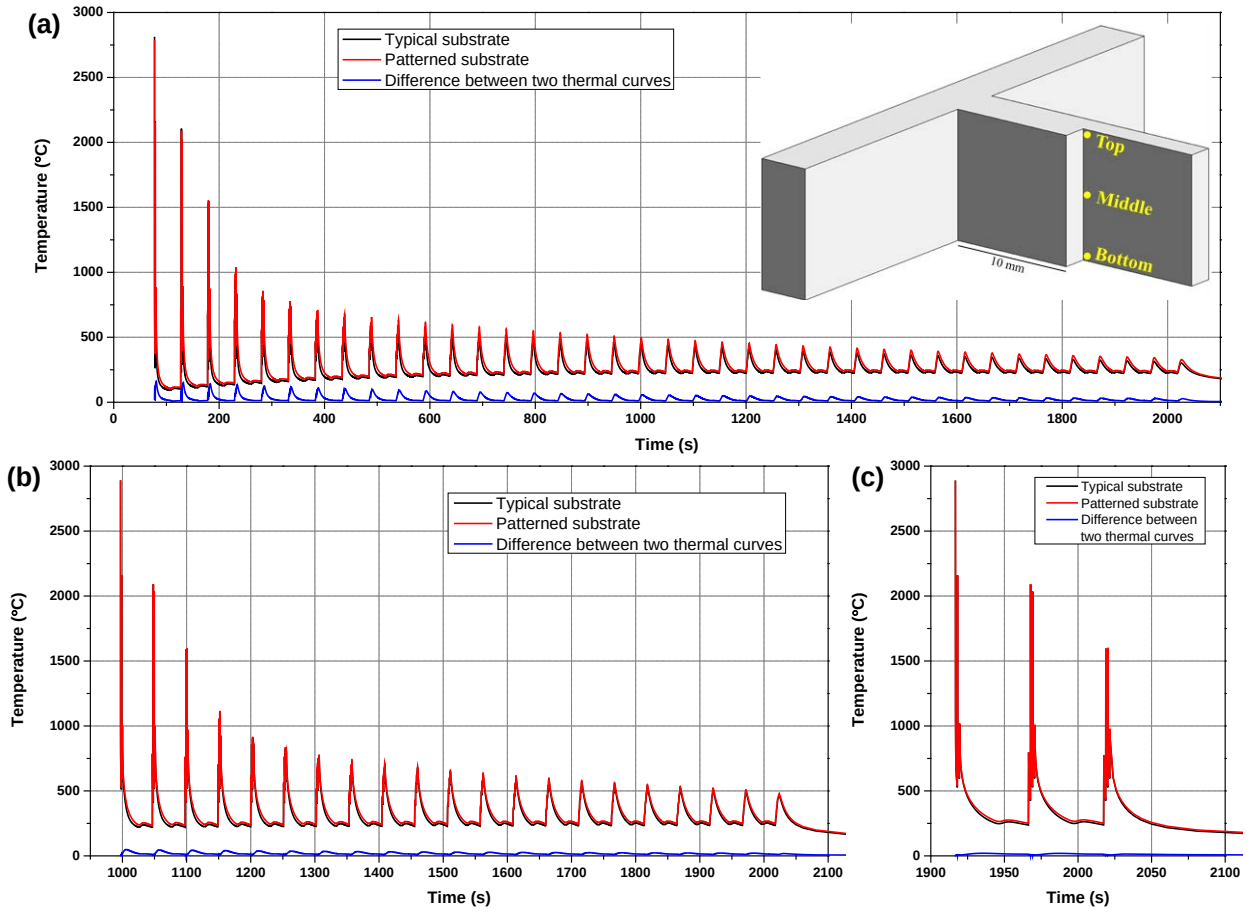

Fig. 13. Predicted thermal histories at different deposit heights of the short-wall of the T-shape build: (a) bottom; (b) middle; (c) top.

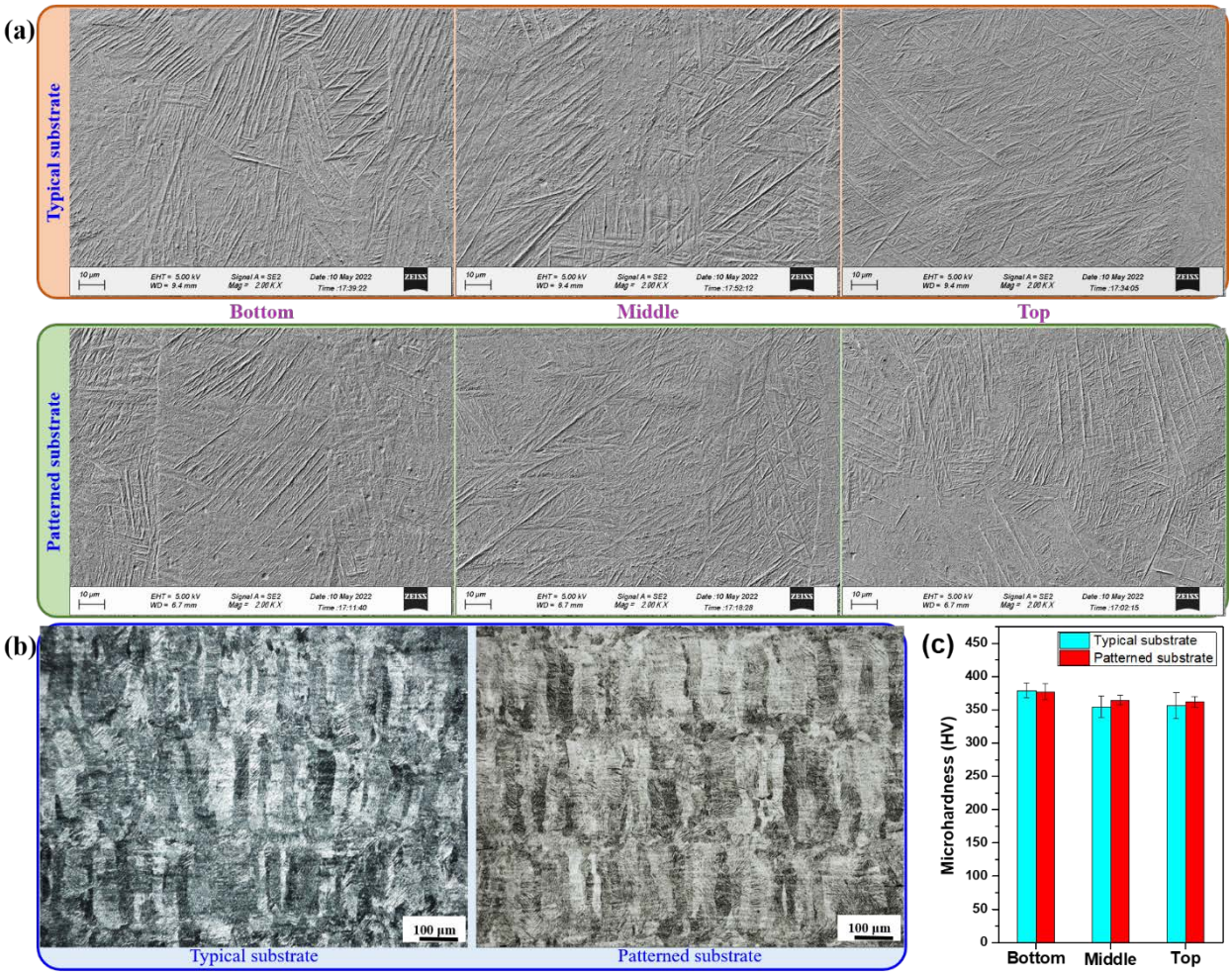

Fig. 14. Comparison of (a,b) microstructures and (c) microhardness in the T-shape deposits.

5 Conclusions

The main conclusions drawn from this work and the general guidelines for mitigating residual stresses in LPBF are as follows:

(1) The thermomechanical FE software is firstly validated with the experimental evidence from a bridge structure fabricated by LPBF. The calculated curling angle (2.76º) induced by the stress relief during the substrate removal process is very close to the measured value of about 2.8º [22]. Thus, the model can be employed to analyze the LPBF process.

(2) In AM, two key factors of MTG and yield temperature are responsible for the generation of residual stresses. Lower MTG or/and higher yield temperature (i.e. weaker mechanical constraint) favor the stress reduction. Based on this, a novel strategy of substrate design to optimize its structural stiffness is proposed to prevent stress accumulations and crack initiation in LPBF processes.

(3) Two T-shape components are printed on two different substrates: without and with grooves. In the former several cracks are observed while the latter is crack-free. The numerical simulation shows a higher stress concentration (up to 1600 MPa) at the bottom ends of the T-shape part when deposited on the typical substrate. However, optimizing the substrate design by adding the proposed groove-pattern successfully mitigates the residual stresses avoiding cracking.

(4) The comparison between the substrate design and the support assistance illustrates that using additional supports instead of a modified substrate design fails to mitigate the stress accumulations at the built basement in LPBF process.

(5) For both typical structures without and with cantilever, using the patterned substrate can efficiently curb the stress development during LPBF process. Noteworthily, the substrate design approach has no significant influence on the metallurgy and microhardness of the build, while this is not the case when the MTG reduction approach is adopted.

(6) The proposed substrate design strategy is easy to apply and cost-effective. It can be applied to improve the printability of metallic materials with high crack sensitivity at the part-substrate interface. Also, it can be combined with the MTG reduction method to avoid cracks when printing more challenging geometries featured by sharp corners where high stress concentrations often occur.

6 Acknowledgments

This work was funded by the Enterprise Ireland project (No. CF-2020-1564-A/B), the National Key R&D Program of China (No. 2016YFB1100100), the European KYKLOS 4.0 project (No. 872570) and the China Scholarship Council (No. 201906290011). The authors also acknowledge the AR-Lab and the AML in TCD.

7 References

[1] Plessis, A., S. Javad, M. Benedetti, S. Murchio, M. Leary, M. Watson, D. Bhate, and F. Berto. 2021. "Properties and applications of additively manufactured metallic cellular materials: a review." Progress in Materials Science: 100918. https://doi.org/10.1016/j.pmatsci.2021.100918

[2] Zhang, W., M. Tong, and N. Harrison. 2019. "Resolution, energy and time dependency on layer scaling in finite element modelling of laser beam powder bed fusion additive manufacturing." Additive Manufacturing 28: 610-620. https://doi.org/10.1016/j.addma.2019.05.002

[3] Huang, H., N. Ma, J. Chen, Z. Feng, and H. Murakawa. 2020. "Toward large-scale simulation of residual stress and distortion in wire and arc additive manufacturing." Additive Manufacturing 34: 101248. https://doi.org/10.1016/j.addma.2020.101248

[4] Mugwagwa, L., I. Yadroitsava, N. Makoana, and I. Yadroitsev. 2021. "Residual stress in laser powder bed fusion." In Fundamentals of Laser Powder Bed Fusion of Metals, 245-276. Elsevier. https://doi.org/10.1016/B978-0-12-824090-8.00014-7

[5] Lu, X., M. Chiumenti, M. Cervera, J. Li, X. Lin, L. Ma, G. Zhang, and E. Liang. 2021. “Substrate Design to Minimize Residual Stresses in Directed Energy Deposition AM Processes.” Materials & Design 202: 109525. https://doi.org/10.1016/j.matdes.2021.109525

[6] Platl, J., S. Bodner, C. Hofer, A. Landefeld, H. Leitner, C. Turk, M. Nielsen, A. Demir, B. Previtali, J. Keckes, and R. Schnitzer. 2022. "Cracking mechanism in a laser powder bed fused cold-work tool steel: The role of residual stresses, microstructure and local elemental concentrations." Acta Materialia 225: 117570. https://doi.org/10.1016/j.actamat.2021.117570

[7] Liu, F., X. Lin, H. Yang, X. Wen, Q. Li, F. Liu, and W. Huang. 2017. "Effect of microstructure on the fatigue crack growth behavior of laser solid formed 300M steel." Materials Science and Engineering: A 695: 258-264. https://doi.org/10.1016/j.msea.2017.04.001

[8] Yu, X., X. Lin, H. Tan, Y. Hu, S. Zhang, F. Liu, H. Yang, and W. Huang. 2021. "Microstructure and fatigue crack growth behavior of Inconel 718 superalloy manufactured by laser directed energy deposition." International Journal of Fatigue 143: 106005. https://doi.org/10.1016/j.ijfatigue.2020.106005

[9] Ueda, Y., H. Murakawa, and N. Ma. 2012. Welding deformation and residual stress prevention. Elsevier.

[10] Lu, X., M. Cervera, M. Chiumenti, and X. Lin. 2021. "Residual Stresses Control in Additive Manufacturing." Journal of Manufacturing and Materials Processing 5(4): 138. https://doi.org/10.3390/jmmp5040138

[11] Zhang, W., M. Tong, and N. Harrison. 2020. "Scanning strategies effect on temperature, residual stress and deformation by multi-laser beam powder bed fusion manufacturing." Additive Manufacturing 36: 101507. https://doi.org/10.1016/j.addma.2020.101507

[12] Hu, Y., X. Lin, X. Yu, J. Xu, M. Lei, and W. Huang. 2017. "Effect of Ti addition on cracking and microhardness of Inconel 625 during the laser solid forming processing." Journal of Alloys and Compounds 711: 267-277. https://doi.org/10.1016/j.jallcom.2017.03.355

[13] Wang, W., W. Lin, R. Yang, Y. Wu, J. Li, Z. Zhang, and Z. Zhai. 2022. "Mesoscopic evolution of molten pool during selective laser melting of superalloy Inconel 738 at elevating preheating temperature." Materials & Design 213: 110355. https://doi.org/10.1016/j.matdes.2021.110355

[14] Wang, Y, X. Lin, N. Kang, Z. Wang, Q. Wang, Y. Liu, and W. Huang. 2022. "Laser powder bed fusion of Zr-modified Al–Cu–Mg

alloy: Crack-inhibiting, grain refinement, and mechanical properties." Materials Science and Engineering: A 838: 142618. https://doi.org/10.1016/j.msea.2022.142618
[15] Svetlizky, D., M. Das, B. Zheng, A. Vyatskikh, S. Bose, A. Bandyopadhyay, J. Schoenung, E. Lavernia, and N. Eliaz. 2021. "Directed energy deposition (DED) additive manufacturing: Physical characteristics, defects, challenges and applications." Materials Today 49: 271-295. https://doi.org/10.1016/j.mattod.2021.03.020
[16] Lu, X., X. Lin, M. Chiumenti, M. Cervera, Y. Hu, X. Ji, L. Ma, and W. Huang. 2019. “In Situ Measurements and ThermoMechanical Simulation of Ti-6Al-4V Laser Solid Forming Processes.” International Journal of Mechanical Sciences 153-154: 119–130. https://doi.org/10.1016/j.ijmecsci.2019.01.043
[17] Cao, J., M. Gharghouri, and P. Nash. 2016. "Finite-element analysis and experimental validation of thermal residual stress and distortion in electron beam additive manufactured Ti-6Al-4V build plates." Journal of Materials Processing Technology 237: 409-419. https://doi.org/10.1016/j.jmatprotec.2016.06.032
[18] Lu, X., X. Lin, M. Chiumenti, M. Cervera, Y. Hu, X. Ji, L. Ma, H. Yang, and W. Huang. 2019b. “Residual Stress and Distortion of Rectangular and S-Shaped Ti-6Al-4V Parts by Directed Energy Deposition: Modelling and Experimental Calibration.” Additive Manufacturing 26: 166–179. https://doi.org/10.1016/j.addma.2019.02.001
[19] Song, X., S. Feih, W. Zhai, C. Sun, F. Li, R. Maiti, J. Wei, Y. Yang, V. Oancea, L. Brandt, A. Korsunsky. 2020. "Advances in additive manufacturing process simulation: Residual stresses and distortion predictions in complex metallic components." Materials & Design 193: 108779. https://doi.org/10.1016/j.matdes.2020.108779
[20] SHIPLEY, H. 2022. "Density Optimisation & In-Situ Microstructure Decomposition of As-Built Selective Laser Melted Ti-6Al-4V." PhD diss., University of Dublin. http://hdl.handle.net/2262/97868
[21] Cheng, L., X. Liang, J. Bai, Q. Chen, J. Lemon, and A. To. 2019. "On utilizing topology optimization to design support structure to prevent residual stress induced build failure in laser powder bed metal additive manufacturing." Additive Manufacturing 27: 290-304. https://doi.org/10.1016/j.addma.2019.03.001
[22] Wang, Z., X. Lin, N. Kang, J. Chen, Y. Tang, H. Tan, X. Yu, H. Yang, and W. Huang. 2021. "Directed energy deposition additive manufacturing of a Sc/Zr-modified Al–Mg alloy: effect of thermal history on microstructural evolution and mechanical properties." Materials Science and Engineering: A 802: 140606. https://doi.org/10.1016/j.msea.2020.140606
[23] Xue, A., X. Lin, L. Wang, X. Lu, H. Ding, and W. Huang. 2021. "Heat-affected coarsening of β grain in titanium alloy during laser directed energy deposition." Scripta Materialia 205: 114180. https://doi.org/10.1016/j.scriptamat.2021.114180
[24] Kruth, J., J. Deckers, E. Yasa, and R. Wauthlé. 2012. "Assessing and comparing influencing factors of residual stresses in selective laser melting using a novel analysis method." Proceedings of the institution of mechanical engineers, Part B: Journal of Engineering Manufacture 226(6): 980-991. https://doi.org/10.1177/0954405412437085
[25] Chiumenti, M., M. Cervera, A. Salmi, C. A. Saracibar, N. Dialami, and K. Matsui. 2010. "Finite element modeling of multi-pass welding and shaped metal deposition processes." Computer methods in applied mechanics and engineering 199(37-40): 2343-2359. https://doi.org/10.1016/j.cma.2010.02.018
[26] Lu, X., M. Chiumenti, M. Cervera, G. Zhang, and X. Lin. "Mitigation of residual stresses and microstructure homogenization in directed energy deposition processes." Engineering with Computers (2022): 1-20. https://doi.org/10.1007/s00366-021-01563-9
[27] Lu, X., X. Lin, M. Chiumenti, M. Cervera, J. Li, L. Ma, L. Wei, Y. Hu, and W. Huang. 2018. “Finite Element Analysis and Experimental Validation of the Thermomechanical Behavior in Laser Solid Forming of Ti-6Al-4V.” Additive Manufacturing 21: 30–40. https://doi.org/10.1016/j.addma.2018.02.003
[28] Chiumenti, M., M. Cervera, N. Dialami, B. Wu, L. Jinwei, and C. Saracibar. 2016. "Numerical modeling of the electron beam welding and its experimental validation." Finite Elements in Analysis and Design 121: 118-133. https://doi.org/10.1016/j.finel.2016.07.003
[29] Chiumenti, M., E. Neiva, E. Salsi, M. Cervera, S. Badia, J. Moya, Z. Chen, C. Lee, and C. Davies. 2017. "Numerical modelling and experimental validation in Selective Laser Melting." Additive Manufacturing 18: 171-185. https://doi.org/10.1016/j.addma.2017.09.002
[30] GiD, The Personal Pre and Post-Processor, CIMNE, Technical University of Catalonia, 2002. https://www.gidsimulation.com/
[31] Ganeriwala, R., M. Strantza, W. King, B. Clausen, T. Phan, L. Levine, D. Brown, and N. Hodge. 2019. "Evaluation of a thermomechanical model for prediction of residual stress during laser powder bed fusion of Ti-6Al-4V." Additive Manufacturing (27): 489-502. https://doi.org/10.1016/j.addma.2019.03.034
[32] Li, C., Z. Y. Liu, X. Y. Fang, and Y. B. Guo. 2018. "On the simulation scalability of predicting residual stress and distortion in selective laser melting." Journal of Manufacturing Science and Engineering 140(4). https://doi.org/10.1115/1.4038893
[33] Zhang, W., M. Tong, and N. Harrison. 2021. "Multipart Build Effects on Temperature and Residual Stress by Laser Beam Powder Bed Fusion Additive Manufacturing." 3D Printing and Additive Manufacturing. https://doi.org/10.1089/3dp.2021.0143
[34] Salem, M., S. Roux, A. Hor, and G. Dour. 2020. "A new insight on the analysis of residual stresses related distortions in selective laser melting of Ti-6Al-4V using the improved bridge curvature method." Additive Manufacturing 36: 101586. https://doi.org/10.1016/j.addma.2020.101586
[35] Strantza, M., R. Ganeriwala, B. Clausen, T. Phan, L. Levine, D. Pagan, J. Ruff, W. King, N. Johnson, R. Martinez, V. Anghel, G. Rafailov, D. Brown. 2021. "Effect of the scanning strategy on the formation of residual stresses in additively manufactured Ti-6Al-4V." Additive Manufacturing 45: 102003. https://doi.org/10.1016/j.addma.2021.102003
[36] Promoppatum, P., and S. Yao. 2020. "Influence of scanning length and energy input on residual stress reduction in metal additive manufacturing: Numerical and experimental studies." Journal of Manufacturing Processes 49: 247-259. https://doi.org/10.1016/j.jmapro.2019.11.020
[37] Hodge, N., R. Ferencz, and R. Vignes. 2016. "Experimental comparison of residual stresses for a thermomechanical model for the simulation of selective laser melting." Additive Manufacturing 12: 159-168. https://doi.org/10.1016/j.addma.2016.05.011
[38] Ahmad, B., S. Veen, M. Fitzpatrick, and H Guo. 2018. "Residual stress evaluation in selective-laser-melting additively manufactured titanium (Ti-6Al-4V) and inconel 718 using the contour method and numerical simulation." Additive Manufacturing 22: 571-582. https://doi.org/10.1016/j.addma.2018.06.002
[39] Zhang, Z., O. Ibhadode, U. Ali, C. Dibia, P. Rahnama, A. Bonakdar, and E. Toyserkani. 2020. "Topology optimization parallel-

computing framework based on the inherent strain method for support structure design in laser powder-bed fusion additive manufacturing." International Journal of Mechanics and Materials in Design 16(4): 897-923. https://doi.org/10.1007/s10999-020-09494-x

[40] Fang, Z., Z. Wu, C. Huang, and C. Wu. 2020. "Review on residual stress in selective laser melting additive manufacturing of alloy parts." Optics & Laser Technology 129: 106283. https://doi.org/10.1016/j.optlastec.2020.106283

[41] Mondal, B., T. Mukherjee, and T. DebRoy. 2022. "Crack free metal printing using physics informed machine learning." Acta Materialia 226: 117612. https://doi.org/10.1016/j.actamat.2021.117612

[42] Cao, Y., X. Lin, N. Kang, L. Ma, L. Wei, M. Zheng, J. Yu, D. Peng, and W. Huang. 2021. " A novel high-efficient finite element analysis method of powder bed fusion additive manufacturing." Additive Manufacturing 102187. https://doi.org/10.1016/j.addma.2021.102187

[43] Zhang, W., F. Liu, F. Liu, C. Huang, H. Zheng, Q. Zhang, Y. Zheng, and J. Gao. 2022. "Microstructural evolution and cracking behavior of Hastelloy X superalloy fabricated by laser directed energy deposition." Journal of Alloys and Compounds 905: 164179. https://doi.org/10.1016/j.jallcom.2022.164179

[44] Song, T., T. Dong, S. Lu, K. Kondoh, R. Das, M. Brandt, and M. Qian. 2021. "Simulation-informed laser metal powder deposition of Ti-6Al-4V with ultrafine α-β lamellar structures for desired tensile properties." Additive Manufacturing 46: 102139. https://doi.org/10.1016/j.addma.2021.102139

[45] Lu, X., G. Zhang, J. Li, M. Cervera, M. Chiumenti, J. Chen, X. Lin, and W. Huang. 2021. "Simulation-assisted investigation on the formation of layer bands and the microstructural evolution in directed energy deposition of Ti6Al4V blocks." Virtual and Physical Prototyping: 1-17. https://doi.org/10.1080/17452759.2021.1942077